Analysis and optimisation of perforated panels making use of metamaterial concepts

Master's Thesis

Author

Gabriela Czupryńska

Tutors

Luís Godinho

ISISE, Departamento de Engenharia Civil, Universidade de Coimbra, Coimbra, Portugal

Jesús Carbajo

DFISTS, Universidad de Alicante, San Vicente del Raspeig, Spain

Cédric Maury

Laboratoire de Mécanique et d'Acoustique (LMA), Marseille, France

Master Waves

Coimbra, Portugal, September 2023

Abstract

Sound-absorbing materials enhance acoustic comfort by controlling reverberation and reducing noise levels. Porous materials like open-cell foams excel at absorbing medium to high frequencies but are less effective at lower frequencies, while resonant structures such as perforated panels offer durability and customization. Such panels normally use simple perforation shapes.

This study focuses on improving sound absorption by exploring panels with varied internal geometries such as tapered, hourglass, inverse-hourglass, perforations with rounded bubble-shaped extensions, and perforations with embedded resonant structures. The influence of rounding the edges and filling the air gap with porous materials is also investigated. An analytical model based on the transfer matrix method and a finite element model are implemented to analyse the systems. The analytical results show good agreement with the FEM results; however, an angle limitation in a tapered perforation case is identified, which can be due to the 1D simplification assumed in the TMM. FE models are used for examining the structures with embedded resonators. Parametric studies are performed to identify the influence of varying geometrical parameters on absorption.

A design method based on optimisation of the geometrical characteristics of a tapered panel is proposed. Three optimal samples with tapered perforations and one with an embedded torus-shaped resonator with arbitrarily chosen dimensions were 3D printed. The samples were experimentally tested using the procedure presented in ISO 10534-2. A good agreement between the predictions and measurement results was found.

Contents

1. Introduction

1.1. Institute for Sustainability and Innovation in Structural Engineering

This dissertation results from a five-month internship at the Faculty of Sciences and Technology of the University of Coimbra. During this time, I was a part of the Functional Performance research group at the Institute for Sustainability and Innovation in Structural Engineering. The Institute is a research and development centre whose areas of interest are different aspects of the performance of civil engineering projects and structures. The acoustic research at the Institute is focused on architectural, building and environmental acoustics. Ongoing works include the development of evaluation methods for railway noise, designing metamaterials for noise control, and developing numerical methods for environmental acoustics.

1.2. Motivation and objectives

Sound-absorbing materials are used in various applications. They can improve acoustic comfort by reverberation time control and noise level reduction. Common types of absorbers are porous materials and perforated panels. Absorption in porous structures results from acoustic energy dissipation due to viscous and thermal effects in the pores [1]. Porous materials such as open-cell foams or fibreglass show good absorptive behaviour over medium and high frequencies. As maximum absorption is achieved at frequencies with wavelengths at least four times larger than the material thickness [2], those materials become inefficient at low frequencies. Moreover, a large amount of porous materials in a room may result in the high frequencies being over-absorbed while the problems related to low frequencies remain. This can be especially disadvantageous in spaces designed for music and speech. Resonant

structures, such as perforated panels, can be used to address these problems. Perforated panel absorbers are based on the concept of a Helmholtz resonator. Compared to porous materials, perforated panels are lightweight, durable, and show persistent performance over time. Moreover, their specific characteristics, such as orifice shape, size, and distribution of the perforations, can be designed to achieve desired absorption characteristics. As numerous materials can be used to make such panels (e.g., wood, metal, acrylic), they offer aesthetic flexibility and can be easily integrated into architectural designs in places such as performance venues, commercial spaces, and industrial facilities [1]. Most commercially used perforated panel absorbers are based on circular or rectangular perforations with straight profiles. Recent advancements in acoustic metamaterials have given valuable insights into the significance of incorporating various shapes and resonant structures into sound-absorbing systems. These concepts offer the potential to enhance the performance of perforated panels.

This work aims to examine the absorptive properties of panels with variable internal geometries. The main goal is to investigate the feasibility of tuning such panels without changing the appearance of the facing. The first part of the work is to analyse analytically and numerically panels with variable cross-sections and with embedded resonant structures. This is followed by proposing a design method based on optimising the geometrical parameters of a panel to tune it to a desired frequency. Finally, the proposed models are verified experimentally.

1.3. Thesis structure

This thesis consists of 5 chapters.

Chapter two provides a theoretical background of perforated panels. It includes models for assessing their acoustic properties and a brief review of recent advances in the field.

Chapter three introduces the methods used in this work. It presents the types of geometries studied. Then, the details of the numerical and analytical models and optimisation methods are shown. Finally, an experimental procedure to verify the proposed models is described.

Chapter four presents the results of the analysis, optimisation and experimental verification.

Chapter five provides the conclusions resulting from this project and proposes future work.

2. Basic concepts and literature review

This chapter will provide a brief review of the literature about perforated panels. Firstly, the theory of a simple Helmholtz resonator is briefly recalled. Then, the first developments in the field of perforated panels are mentioned, followed by recent advancements.

2.1. Helmholtz resonator

The concept of a Helmholtz resonator is simple and has been described in various works [3] [4]. Such a resonator consists of a rigid cavity of volume V connected to a neck of length l and a cross-section area of S (see Fig. 2.1).
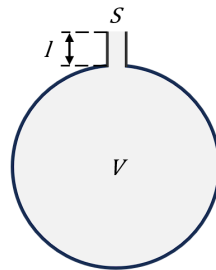
Figure 2.1: Schematic representation of a Helmholtz resonator

If the dimensions are small compared to the wavelength of the incident sound wave, the system can be described as a mass-spring model [5]. The mass is analogous to the air in the neck, while the spring is the air in the interior of the cavity, which is periodically compressed and expanded. The resonance frequency of such a system is:

$$\omega_{res} = c_0 \sqrt{\frac{S}{l \cdot V}} \tag{2.1}$$

where c_0 is the velocity of sound in air. The resonator can be adjusted to absorb sound at a

desired frequency by varying the cavity volume or neck size. Consequently, sound absorption at low frequencies can be achieved without significantly increasing the resonator size.

The energy dissipation in a resonator is mainly associated with viscous and thermal losses on the surfaces [4]. Those losses occur in thin layers: viscous and thermal boundary layers whose widths are, respectively [6]:

$$\delta_V = \sqrt{\frac{2\eta}{\rho_0 \omega}} \tag{2.2}$$

and

$$\delta_T = \sqrt{\frac{2\kappa}{\rho_0 \omega C_P}} \tag{2.3}$$

where μ is the viscosity coefficient of air, κ is the thermal conductivity of air and C_P is the heat capacity of air at constant pressure.

2.2. Perforated panels

A perforated panel can be described as a distributed Helmholtz resonator. In such cases, the perforations act as necks, and each opening corresponds to a cavity volume determined by the spacing between perforations. A schematic representation of a perforated panel absorber is shown in Fig. 2.2. Early works of Crandall [7] and Rayleigh [3] on sound propagation in circular ducts allow for the derivation of an expression for the specific acoustic impedance Z of a panel with circular perforations [8]:

$$Z = j\omega\rho_0 t \left[1 - \frac{2}{x\sqrt{-j}} \frac{J_1(x\sqrt{-j})}{J_0(x\sqrt{-j})} \right]^{-1} \tag{2.4}$$

where $x = R\sqrt{\frac{\omega\rho_0}{\eta}}$, η is the dynamic viscosity of air, and J_0, J_1 are Bessel functions of the first kind and the zeroth and first order, respectively. The parameter x, or perforate constant, can be also approximated by $x = \sqrt{2}\frac{R}{d_v}$, where d_v is the thickness of the viscous boundary layer [9].
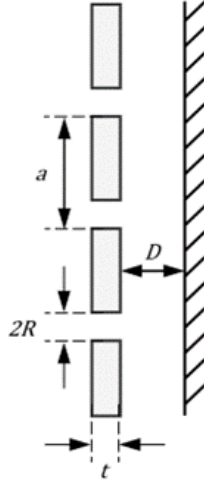
Figure 2.2: Schematic representation of a perforated panel

Early research focused on perforated sheets acting as protective facings for porous materials. An approximate analysis of this case was carried out by Bolt [10]. He showed that the acoustic impedance of the perforated facing could be represented in terms of surface porosity, hole diameter and plate thickness. This theory was further developed and backed by experimental results by Ingard and Bolt [11]. The concept of microperforated panels (MPPs) was proposed by Maa in 1975 [9]. It combined Crandall's sound propagation model in small circular tubes [7] and resistive end corrections proposed by Ingard [4]. This theory suggests that reducing the size of the perforations to submillimetre, thus increasing viscous losses in the holes, allows for excellent absorption properties over relatively broad frequency ranges. Further analysis of the wideband capabilities of MPPs was performed using double-layer systems [12].

Further research included work on determining the transfer impedance of panels with non-circular cross-sections. Stinson [13] expanded the model of Crandall to determine the propagation characteristics of tubes with arbitrary cross-sections. Their specific acoustic impedance can be written as:

$$Z_s = j\omega\rho_0 t \left[1 - \frac{\tanh\left(x_s\sqrt{j}\right)}{x_s\sqrt{j}}\right]^{-1}, \tag{2.5}$$

where $x_s = \frac{w}{2}\sqrt{\frac{\omega\rho_0}{\eta}}$, and w is the width of the perforation.

A new method of analysing perforated panels was proposed by Atala and Stinson [14]. It was shown that such panels can be modelled as equivalent fluids with effective tortuosity. This tortuosity is found to depend on radiation corrections and the dynamic tortuosity of the interfacing media. The model provides descriptions of macro- and microperforated panels and has been verified experimentally.

2.3. Innovative designs

Advancements in manufacturing methods, e.g., the introduction of affordable 3D-printing technologies, allow for producing panels with more complicated internal geometries. Recent studies, through innovative methodologies, numerical simulations, and experimental validations, provide valuable insights into such panels' design, prediction, and optimisation.

Several themes present in recent research will be presented next. The first one is the parallel arrangement of panels with variable properties and the introduction of rigid partitions between them. In [15], two configurations are examined: one being four perforated panels with each perforation being extended by a tube in the air cavity (perforated panels with extended tubes - PPETs, see Fig. 2.3e), and the other being three PPETs and one micro-perforated panel. Both structures are a result of optimisation for the absorption coefficient. The low-frequency performance of the proposed panels is excellent, with the latter covering a broader frequency band. An extension of the parallel arrangement is introducing non-rigid partitions. In [16], the implementation of micro-perforated partitions was analysed (the structure shown in Fig. 2.3a). The panels' performance was assessed with the equivalent circuit method and verified with finite element (FE) simulations. The results suggest that the microperforated partitions offer potential for broadband absorption compared to rigid ones. Similarly, in [17], porous partitions were used. This study introduced an FE model for this type of structure. The analysis performed by the authors suggested an increase in the bandwidth of high absorption when porous material with high flow resistivity is used instead of a rigid partition.

Another theme is combining different types of absorbing structures or materials. An example of this approach can be grooved panels presented in [20], or panels with step-wise apertures (PPSAs) proposed in [23]. The grooved panel described in the former work con-
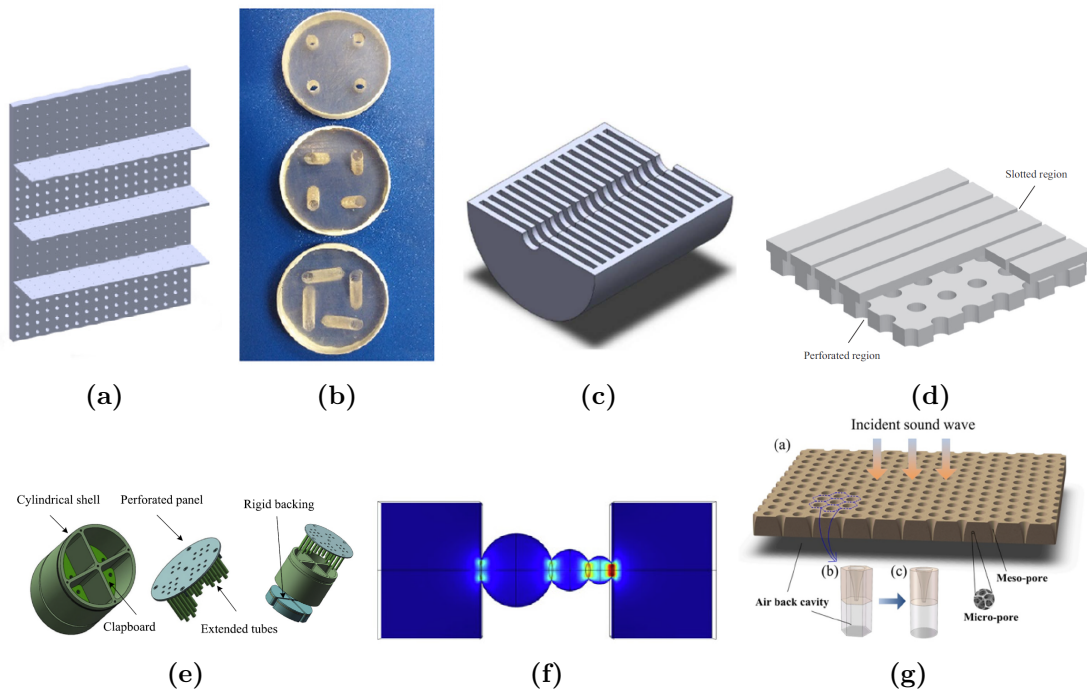
Figure 2.3: Examples of innovative perforated panels: (a) panel with microperforated partitions [16]; (b) panel with oblique perforations [18]; (c) perforation with embedded cylindrical cavities [19];(d) grooved acoustic panel [20]; (e) parallel assembly of perforated panels with extended tubes [15]; (f) graded spherical perforations [21]; (g) porous material with tapered perforations [22].

sists of two surfaces, one with slits and the other with circular perforations (see Fig. 2.3d). An analytical description based on the transfer matrix method and the Johnson-Champoux-Allard model was developed and used for parametric studies. The results show the influence of the sizes of the openings as well as the thicknesses of the panels on absorption and can act as guidelines for design. PPSAs consist of two surfaces with coaxial circular perforations of different sizes. Such panels offer an increase in absorption compared to single-layer perforated panels. A further example of combining various types of absorbers is metaporous concrete presented in [24], where the absorptive characteristics of porous concrete are enhanced by an embedded resonator and modelled using the equivalent-fluid method. The described solution not only offers extra absorption in low frequencies due to the resonant behaviour but also can be used in outdoor applications. Another example is a porous material with tapered perforations backed by an air cavity presented in [22] (see Fig. 2.3g. An analytical model based on the double porosity theory was developed, and the tapered shape was accounted for

by dividing the panel into layers. This solution offers excellent absorptive properties over a broad low-frequency band.

Finally, it is worth mentioning that research has been developed concerning perforated panels with innovative perforation shapes. In [18], oblique perforations were proposed (see Fig. 2.3b. The oblique shape results in an extension of the effective length of the perforation without changing the thickness of the panel. An analytical model based on the equivalent-fluid theory was developed and verified with FEM and experimentally. It was shown that by proper choice of the geometrical parameters of such panels, an increase in absorption and frequency shift to lower frequencies are possible. In [19], a structure with a lattice of cylindrical cavities embedded in the thickness of the panel (see Fig. 2.3c is proposed. Based on an analytical model and experimental verification, it was proven that such a structure allows for a significant reduction in panel thickness or the absorption peak appearing at a lower frequency compared to a straight perforation. Other geometries investigated included: tapered micro-perforations [25], [26]; spherical perforations [21] (geometry shown in Fig. 2.3f; horn-shaped microperforations [27]; and hourglass-shaped perforations [28]. In most of these studies, the geometrical characteristics of the panels were arbitrarily chosen. The panels are often analysed numerically, and samples are produced to verify the numerical models.

3. Methods

In this chapter, the methods used in this work are introduced. The analytical and numerical methods for variable cross-section perforations are presented. Then, the optimisation algorithm used for design is outlined. These are followed by a description of the experimental procedure used for the models' validation.

3.1. Analytical estimation of absorption coefficient

The method of evaluating the absorption coefficient of a perforated panel absorber is based on the transfer matrix method (TMM). TMM is a powerful analytical tool for modelling systems that can be reduced to one dimension. Various problems can be described using TMM, including reflection and transmission in multilayered media. It allows for fast calculations even for complicated structures and enables straightforward implementation of optimisation techniques [29].

A given system consisting of arbitrary layers under the hypothesis of plane wave propagation can be described using a transfer matrix. This matrix relates sound pressure and normal particle velocity on both sides of the system (points 0 and 1 in Fig. 3.1) [29]:

$$\begin{bmatrix} p(0) \\ v(0) \end{bmatrix} = [T] \begin{bmatrix} p(1) \\ v(1) \end{bmatrix} = \begin{bmatrix} t_{11} & t_{12} \\ t_{21} & t_{22} \end{bmatrix} \begin{bmatrix} p(1) \\ v(1) \end{bmatrix}. \tag{3.1}$$

$[T]$ is a total transfer matrix which is given by the product of transfer matrices of each layer in the system:

$$[T] = \prod_{i=0}^{N} [T]_i. \tag{3.2}$$

The transfer matrix of a fluid layer (air gap or a layer of porous material modelled using the equivalent fluid method) can be written as:
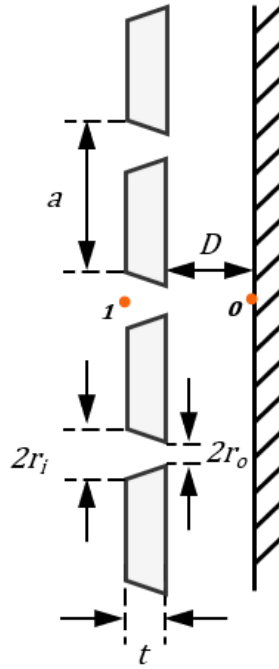
$$[T]_f = \begin{bmatrix} \cos(k_f D) & iZ_{c,f}\sin(k_f D) \\ \frac{i}{Z_{c,f}}\sin(k_f D) & \cos(k_f D) \end{bmatrix}, \tag{3.3}$$

where $Z_{c,f}$ is the characteristic impedance and k_f is the wave number in the fluid layer.

The transfer matrix of a perforated panel can be established as follows:

$$[T]_p = \begin{bmatrix} 1 & Z_p \\ 0 & 1 \end{bmatrix}, \tag{3.4}$$

where Z_p is the acoustic impedance of the perforated panel.

Figure 3.1: Schematic illustration of an acoustic absorber with a panel with tapered perforations

As the perforations in the panels under study are periodically arranged, the panel's properties can be analyzed by only considering a single unit cell. A square unit cell with side length a is considered in further analysis. The variable radius of the perforation is accounted for by dividing the unit cell into multiple layers and approximating the perforation in each layer with a cylinder (see Fig. 3.2). The perforated panel is therefore modelled as a multilayered

system consisting of N panels of thickness $t_i = t/N$. The volume of each cylinder equals the volume of the tapered perforation in each layer. As the number of layers increases, the model converges to one solution. For the geometries studied in this work, it was found that around 30 layers are optimal for the result and computational time.
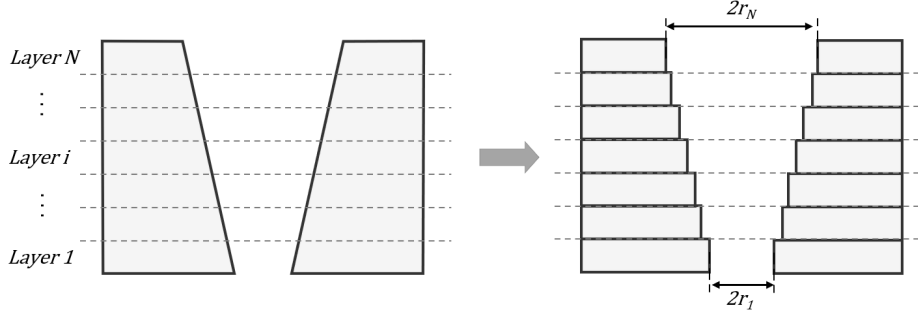
Figure 3.2: Schematic illustration of the process of dividing a perforation into equivalent layers

To calculate the specific acoustic impedance Z_p of a panel with circular perforations, the formula provided in Eq. 2.4 is applied to each layer. For slitted panels, the formula used is presented in Eq. 2.5.

To account for additional dissipation at the inlet and outlet of the perforations, surface resistance and a correction for reactance are added to the specific acoustic impedance of the initial and final layers [8]:

$$Z_{end} = \frac{1}{\epsilon}(2\sqrt{2\omega\rho_0\eta} + i\omega\rho_0\delta), \tag{3.5}$$

with δ being added length, which depends on the perforation cross-section shape. For circular perforations δ_c takes form of [8]:

$$\delta_c = 0.48\sqrt{\pi R^2}(1 - 1.14\sqrt{\epsilon}). \tag{3.6}$$

For slits δ_s is [30]:

$$\delta_s = \frac{1}{\pi}w \cdot \log\sin\left(\frac{\pi\epsilon}{2}\right). \tag{3.7}$$

The perforation ratio ϵ is $\epsilon_c = \frac{\pi R^2}{a^2}$ in the case of circular perforations and $\epsilon_s = \frac{R}{a}$ in the case of slits.

Porous materials' properties are described using the Delany-Bazley-Miki model. It is an empirical model in which the complex wavenumber k and characteristic impedance Z_c depend on the angular frequency ω and the material's flow resistivity σ.

The formulas for k and Z_c are [31]:

$$k(\omega) = k_0 \left[1 + 0.109 \left(\frac{\rho_0 \omega}{2\pi\sigma} \right)^{-0.618} + 0.16i \left(\frac{\rho_0 \omega}{2\pi\sigma} \right)^{-0.618} \right], \qquad (3.8)$$

and

$$Z_c(\omega) = Z_0 \left[1 + 0.07 \left(\frac{\rho_0 \omega}{2\pi\sigma} \right)^{-0.632} + 0.107i \left(\frac{\rho_0 \omega}{2\pi\sigma} \right)^{-0.632} \right]. \qquad (3.9)$$

3.2. Numerical estimation of absorption coefficient

The numerical method used in this work is the finite element method (FEM) implemented in the commercial software COMSOL Multiphysics [32]. The models were solved for acoustic pressure in the frequency domain.

A single unit cell of each absorber was modelled, including a portion of free-field above it. In the case of circular perforations, the models were 2D-axisymmetric (an example shown in Fig. 3.3a). In instances where FEM models were compared to the analytical ones, the radius of the circular unit cell was chosen so that the cell's surface was the same as in the case of the square unit cell. The primary boundary condition used in the model is a rigid boundary (hard wall). It was used at the surfaces where the viscothermal losses could be neglected and at the boundaries of the model. This condition specifies that the component of the particle velocity normal to the surface equals zero. At the system's inlet, a *port* boundary condition implemented in COMSOL Multiphysics was applied. This boundary condition serves two purposes: establishing a non-reflecting condition at the waveguide's end (outlet) and introducing an incident wave at a boundary (source). It allows for modelling acoustic waves entering and leaving the system. It is assumed only plane waves impinge on the surface of the panel. To include thermal and viscous losses along the surfaces of the perforations, the boundary layer impedance (BLI) condition was used, with the expression [33]:

$$-\delta_V \frac{i-1}{2}\Delta_\parallel p + \delta_T k^2 \frac{(i-1)(\gamma-1)}{2}p + \frac{\partial p}{\partial n} = 0, \qquad (3.10)$$

where $\Delta_\parallel$ is the sum of the second-order spatial derivatives in the tangent directions, n is the boundary normal component, δ_V and δ_T are the viscous and thermal boundary layer thicknesses, defined in Eqs. 2.2 and 2.3, respectively. This boundary condition is valid unless the boundary layers overlap [33], which is not the case in this study.

(a)   **(b)**
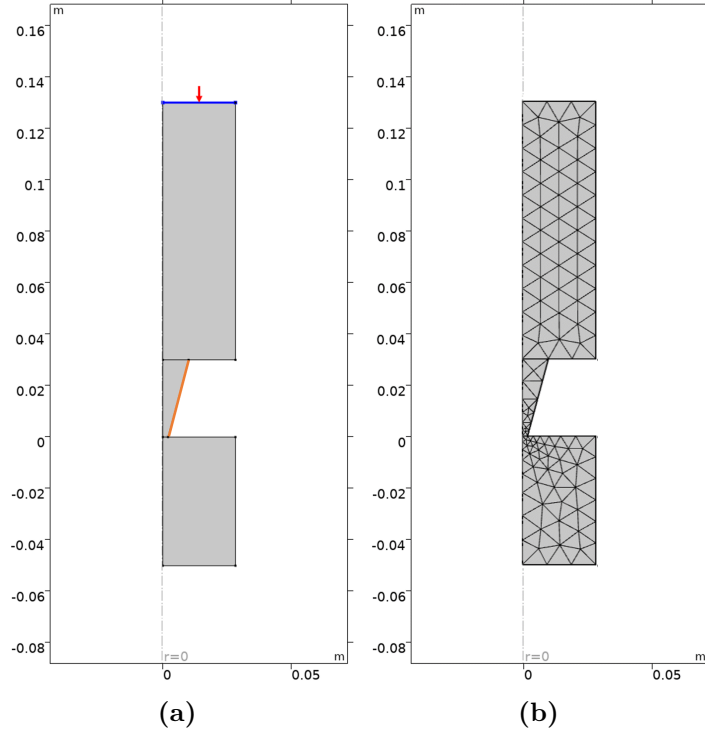
Figure 3.3: (a) An example of a geometry implemented in COMSOL Multiphysics, marked in blue - *port* boundary condition, marked in orange - BLI condition, (b) an example of a mesh used for simulations.

Incident pressure was assigned at the inlet of the system. To enable calculations using the values characterizing the incident and reflected fields, *port* boundary condition was used. The reflection coefficient was defined as

$$R = \frac{P_{out}}{P_{inc}}, \qquad (3.11)$$

where P_{out} is the power of the outgoing mode and P_{inc} is the power of the incident mode. The absorption coefficient was then calculated as

$$\alpha = 1 - R. \tag{3.12}$$

A triangular mesh was used for 2D models, and a tetrahedral mesh for 3D ones. The maximum size of the mesh element was set so that there are at least ten elements per wavelength at the largest frequency in the model. An example of a mesh is shown in Fig. 3.3b. The results were compared to those calculated using a finer mesh for at least one case in each type of geometry. It was verified that the discretisation was correct, as the difference between the results was insignificant.

3.3. Optimisation

As the behaviour of the studied absorbers depends on their various geometrical characteristics, optimisation was used to design systems tuned to arbitrarily chosen frequency bands. An optimisation problem can be described mathematically as [34]:

$$
\begin{aligned}
\underset{x}{\text{minimise}} \quad & F(x) \\
\text{subject to} \quad & h(x) = 0, \\
& g(x) \geq 0,
\end{aligned}
\tag{3.13}
$$

where $F(x)$ is the objective function and $h(x)$ and $g(x)$ are the constraint functions.

In this study, the interior point algorithm proposed in [35] was used as it was implemented in MATLAB optimisation Toolbox [36]. The method's name refers to the fact that the algorithm works by iteratively searching for solutions in the interior of the feasible region restricted by the constraints.

The main problem is divided into a sequence of approximate unconstrained problems, and each subproblem takes the form [35]:

$$
\begin{aligned}
\underset{x,s}{\text{minimise}} \quad & F_\mu(x) - \mu \sum_{i=1}^{m} \ln s_i \\
\text{subject to} \quad & h(x) = 0, \\
& g(x) + s = 0,
\end{aligned}
\tag{3.14}
$$

where μ is the barrier parameter and s_i are positive slack variables. The added logarithmic function is named a barrier function, and its role is to reinforce the constraints of the main problem while solving the unconstrained subproblems. Each subproblem corresponds to one value of μ. The slack variables, introduced to convert the inequality constraints to equality constraints, are positive to keep the iterates inside the feasible region. As the value of μ decreases towards zero, the minimum of the objective function F is approached.

3.4. Experimental setup

To validate the proposed models, the normal incidence absorption coefficient of the samples was measured using the standard procedure presented in ISO 10534-2 [37]. The setup consists of a cylindrical tube, a sample mounted on one end of the tube and a loudspeaker on the other, and two microphones located at distances x_1 and x_2 from the sample (see. Fig. 3.4).
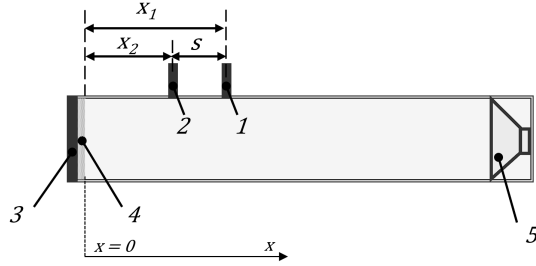
Figure 3.4: Schematic representation of an impedance tube setup for normal incidence absorption coefficient measurement; 1 - microphone 1, 2 - microphone 2, 3 - rigid termination, 4 - sample, 5 - loudspeaker.

The sound field in the tube consists of the incident waves and the waves reflected by a sample under test. At the boundary of the sample ($x = 0$) the total sound pressure is [37]:

$$p(x) = p_{I(x=0)}e^{ikx} + p_{R(x=0)}e^{-ikx}, \tag{3.15}$$

where $p_{I(x=0)}$ and $p_{R(x=0)}$ are the amplitudes of the pressure of the incident and reflected waves, respectively. Similarly, the pressures at the two microphone positions are:

$$p(x = x_1) = p_{I(x=0)}e^{ikx_1} + p_{R(x=0)}e^{-ikx_1} \tag{3.16}$$

and

$$p(x = x_2) = p_{I(x=0)}e^{ikx_2} + p_{R(x=0)}e^{-ikx_2}. \tag{3.17}$$

The transfer functions H_I for the incident, and H_R for the reflected waves are:

$$H_I = \frac{p_{I(x=x_2)}}{p_{I(x=x_1)}} = e^{-ik(x_1-x_2)} = e^{-iks} \tag{3.18}$$

and

$$H_R = \frac{p_{R(x=x_2)}}{p_{R(x=x_1)}} = e^{ik(x_1-x_2)} = e^{iks}, \tag{3.19}$$

where $s = x_1 - x_2$ is the distance between the microphones.

The transfer function considering the total sound field is:

$$H_{12} = \frac{p_{(x=x_2)}}{p_{(x=x_1)}} = \frac{p_{I(x=0)}e^{ikx_2} + p_{R(x=0)}e^{-ikx_2}}{p_{I(x=0)}e^{ikx_1} + p_{R(x=0)}e^{-ikx_1}} = \frac{e^{ikx_2} + re^{-ikx_2}}{e^{ikx_1} + re^{-ikx_1}}, \tag{3.20}$$

with $r = \frac{p_{R(x=0)}}{p_{I(x=0)}}$ being the complex reflection coefficient. Combining Eqs. 3.18, 3.19 and 3.20 gives an expression for r:

$$r = \frac{H_{12} + H_I}{H_R - H_{12}}e^{2ikx_1}. \tag{3.21}$$

The normal incidence sound absorption coefficient is:

$$\alpha = 1 - |r|^2. \tag{3.22}$$

4. Models under study

This chapter presents the geometries of the structures that were the subject of the study. Except for the model described in Sec. 4.1.2, all panels are backed by an air gap.

4.1. Tapered circular perforations

4.1.1. Perforations backed by an airgap

A tapered perforation with the inlet radius larger than the outlet radius is shown in Fig. 4.1. θ was defined as the angle between the perforation surface and the normal to the panel. The tapered panels were investigated in two orientations: with the inlet larger than the outlet and the reverse.
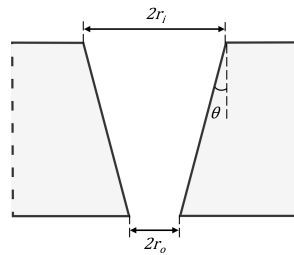
Figure 4.1: Schematic representation of a tapered perforation

### 4.1.2. Porous material in the cavity

The panel's geometry is the same as in Sec. 4.1.1. The space between the panel and the rigid backing is filled with a porous material. Two materials were used: Rockwool with the flow resistivity $\sigma = 7000 \frac{N \cdot s}{m^4}$ and melamine foam with $\sigma = 12200 \frac{N \cdot s}{m^4}$.

4.2. Tapered slits

The cross-section of a panel with tapered slits is the same as in Fig. 4.1. The panel is assumed to be infinitely long.

4.3. Perforations with rounded edges

This geometry is a tapered perforation with rounded edges modelled as fillets (see Fig. 4.2). The fillet radii r_{fil_i} and r_{fil_o} were linked to the inlet and outlet radii (e.g. $R_{fill\_i} = 3/4r_i$). This structure was investigated only with FEM.
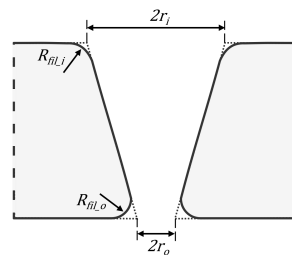
Figure 4.2: Schematic representation of a tapered perforation with rounded edges

4.4. Hourglass-shaped perforations

To investigate the influence of end corrections on the panels' performance, hourglass-shaped and inverse-hourglass-shaped perforations were studied. The geometrical characteristics of these structures are (see Fig. 4.3): r_i - inlet radius, r_{min} - radius at half of the thickness of an hourglass-shaped perforation, r_{max} - radius at half of the thickness of an inverse-hourglass-shaped perforation.
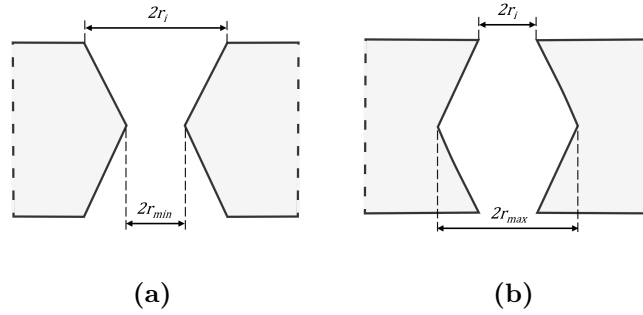
Figure 4.3: Schematic representation of (a) an hourglass-shaped perforation and (b) an inverse-hourglass-shaped perforation

4.5. Bubble-shaped perforations

This geometry involves a rounded expansion in the thickness of the perforation. To model this structure, a one-dimensional multi-quadratic radial basis function (MQ RBF) was used in the form of [38]:

$$f(r) = \sqrt{r^2 + c^2}, \tag{4.1}$$

where r is the distance from a reference point, and c is a scalar shape parameter. This formulation allows for the approximation of the shape along a domain based on a finite number of known points. The points used to approximate the "bubble" shape were marked in orange in Fig. 4.4. The shape parameter value used for the modelling was 0.01. This value allowed for the best approximation of the desired shape.
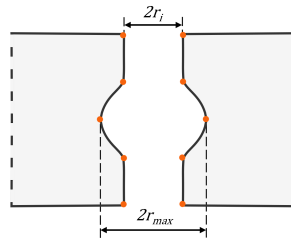
Figure 4.4: Schematic representation of a bubble-shaped perforation

4.6. Embedded resonant structure

Two structures with resonators embedded in their thicknesses were investigated: one with a torus-shaped resonator and one with two pairs of spherical resonators. Both systems were analysed with FEM. The former was modelled as a 2D axisymmetric system, and the latter as a 3D one.

4.6.1. Torus-shaped resonator

A resonator, whose part referred to as neck in 2.1 is a cylinder, and the volume is a torus, is connected to the perforation. The geometrical characteristics of this structure are (see Fig. 4.5): r_i - radius of the perforation, w_{HR} - width of the "neck", l_{HR} - length of the "neck", r_{HR} - inner radius of the torus.
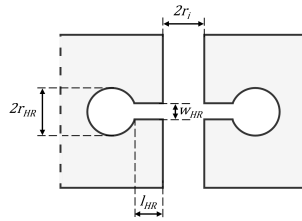
Figure 4.5: Schematic representation of a perforation with an embedded torus-shaped resonator

4.6.2. Spherical resonator

Two pairs of spherical resonators are connected to the perforation. The resonators have the same cylindrical necks and different radii of the volume. The geometrical characteristics of this structure are (see Fig. 4.6): r_i - radius of the perforation, w_{HR} - width of the "neck", l_{HR} - length of the "neck", r_{HR1}, r_{HR2} - radius of the volumes of the resonators.
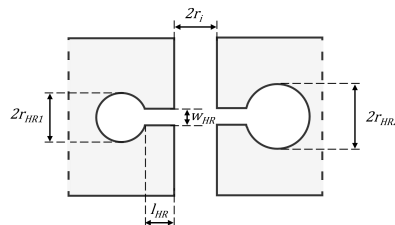
Figure 4.6: Schematic representation of perforation with embedded spherical resonators

5. Results and discussion

5.1. Analytical and numerical study

The outcomes of the analytical and numerical investigations for the geometries described in Chap. 4 are presented below.
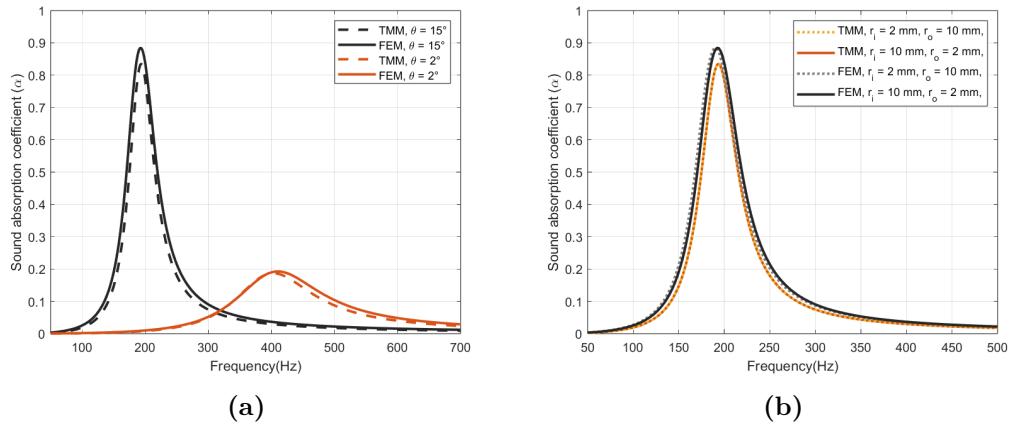
Figure 5.1: Sound absorption of panels with tapered perforations: (a) TMM and FEM results for two panels; (b) TMM and FEM results for a single panel in two configurations: $r_i > r_o$ and $r_o > r_i$.The geometrical characteristics of the panels are presented in Table A.1 in Appendix A.

5.1.1. Tapered circular perforations

The analytical model described in Sec. 3.1, which was validated against a FEM model (see Sec. 3.2), demonstrates satisfactory results. However, this model exhibits a limitation. Fig. 5.2 shows results for panels whose geometrical parameters are listed in Table A.1 in Appendix A. It can be noticed that the accuracy of the analytical calculations compared to FEM decreases as θ increases. This effect can be attributed to the fact that for larger θ, the assumption of one dimension no longer holds, and a more elaborate model is necessary. Due

to this limitation, a limit of $\theta \leq 25°$ was considered in further analysis. The analytical and numerical results within the angle limit (see Fig. 5.1a) show good agreement. In Fig. 5.1b, results for one panel are shown: in the original configuration and inverted. Interestingly, there is no difference between those two orientations. A similar effect was reported in [25] and [26]. In [26], it is suggested that this behaviour is due to the lack of non-linear effects.

Figure 5.2: Sound absorption of panels with tapered perforations: TMM and FEM results for different values of θ. Solid line - finite element model, dashed line - analytical model. The geometrical characteristics of the panels are presented in Table A.1 in Appendix A.

5.1.2. Tapered perforations with porous material in the cavity

Introducing a porous material into the backing cavity results in a slight shift of the absorption peak towards low frequencies and increased absorption. Additionally, the absorption bandwidth widens slightly. In Fig. 5.3, this effect is shown for the tapered and straight perforations, which is the same in both cases. The type of porous material has no influence in the analysed cases.

5.1.3. Tapered slits

In the case of tapered slits, the results of the analytical model are satisfactory. In Fig. 5.4a, it can be noticed that discrepancies between the TMM and FEM models occur. This can be attributed to the fact that in the analytical calculations, the panel and the slits are assumed laterally infinite, while in the FEM simulation, a 3D panel of finite length is considered.
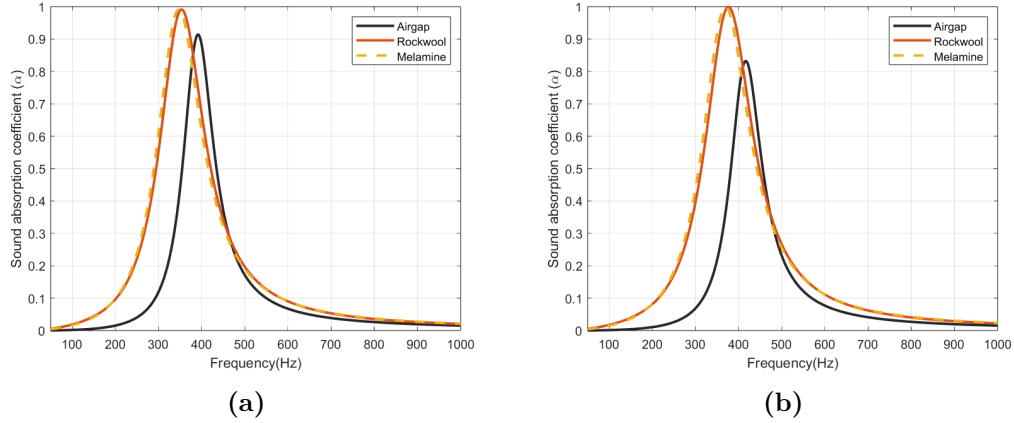
Figure 5.3: Sound absorption of panels backed by porous materials: (a) tapered perforation; (b) straight perforation. The geometrical characteristics of the investigated panels are presented in Table A.2 in Appendix A.
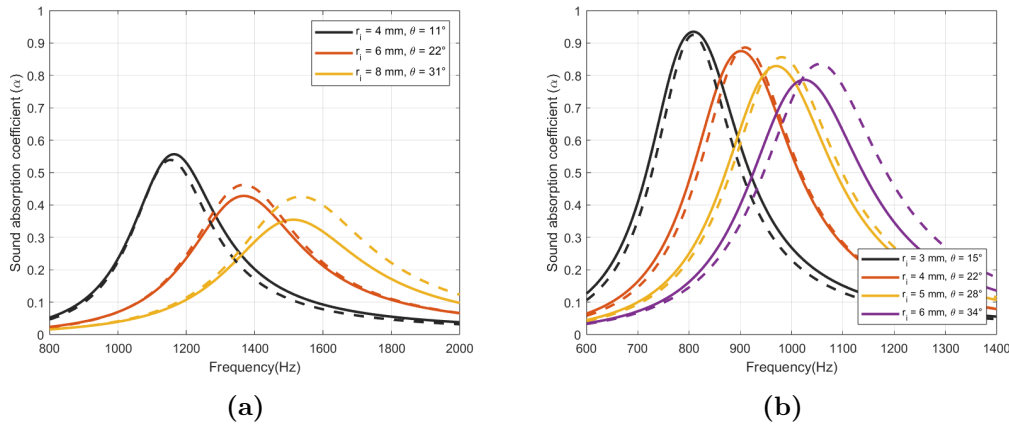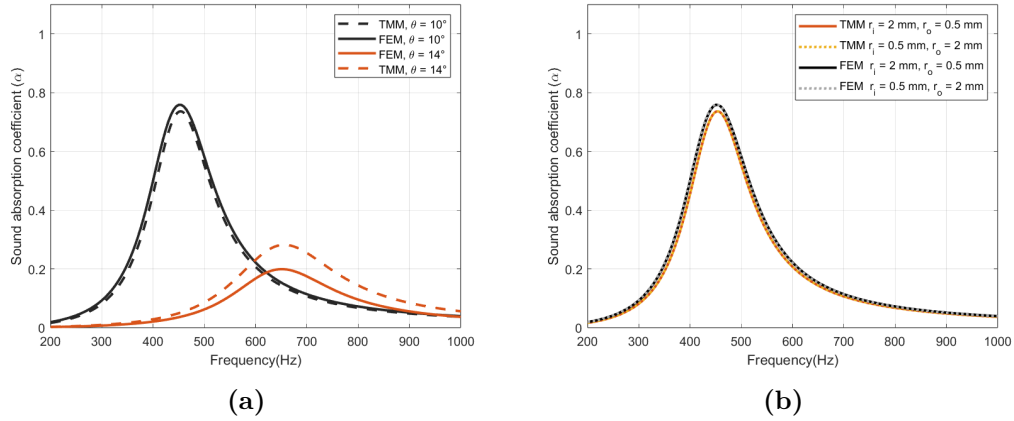

Figure 5.4: Sound absorption of panels with tapered slits: (a) TMM and FEM results for two panels; (b) TMM and FEM results for a single panel in two configurations: $w_i > w_o$ and $w_o > w_i$. The geometrical characteristics of the examined panels are shown in Table A.3 in Appendix A.

5.1.4. Perforations with rounded edges

Two ways in which the rounding of the edges can influence the panel were investigated: the size of the fillet (with both inlet and outlet edge being rounded) and rounding the inlet or outlet vs. both. Those behaviours were investigated for tapered and straight cases. This study was carried out only using FEM simulations, as in the case of the analytical method, the angle limitation described in 5.1.1 would have been violated.
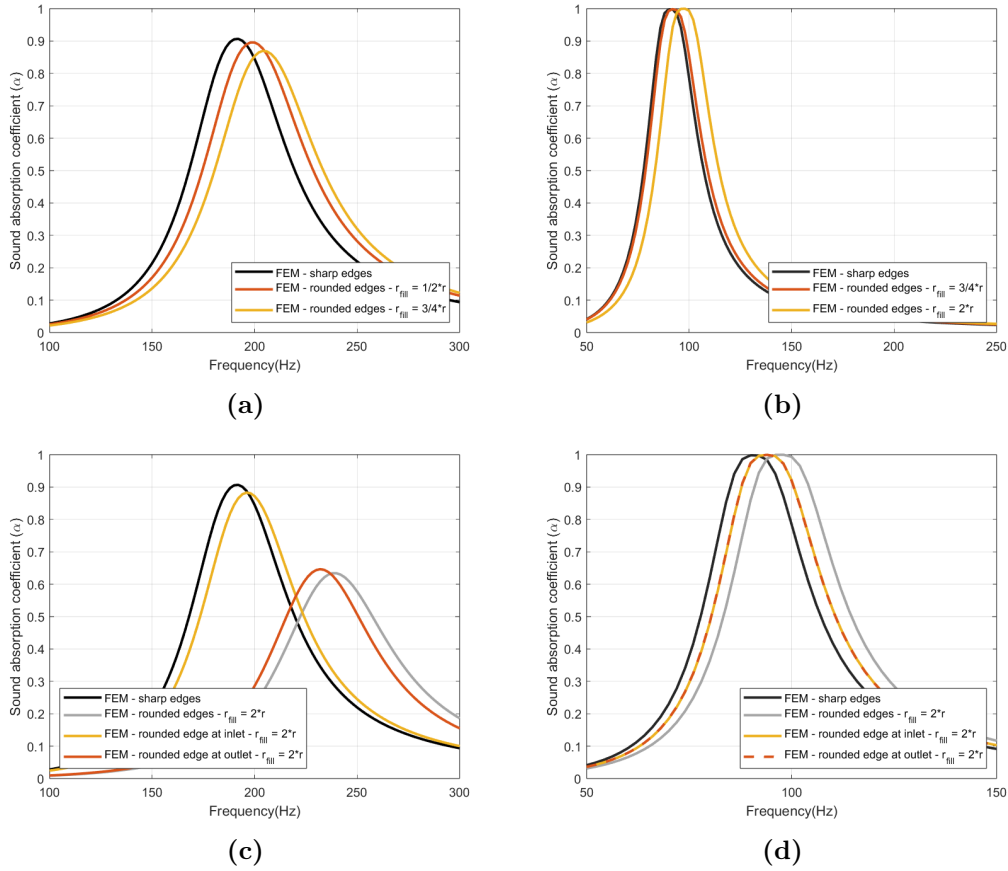
Figure 5.5: Sound absorption of panels with rounded edges: influence of fillet size for (a) tapered and (b) straight perforations; the influence of rounding the inlet and/or outlet for (c) tapered and (d) straight perforations. The geometrical characteristics of the panels examined are presented in Table A.4 in Appendix A.

In Fig. 5.5a, it can be seen that a fillet whose radius is a fraction of the radius of the perforation influences the result. Rounding the edges results in a decrease in absorption and a shift of the absorption peak to a higher frequency. Meanwhile, in the straight perforation case shown in Fig. 5.5b, a large fillet is necessary to observe any influence on the result. In this situation, no absorption decrease was observed. The peak has shifted towards higher frequencies. To observe the influence of rounding the inlet or outlet vs. both, the fillet radius was maintained the same in relation to the perforation radius. In Fig. 5.5c, where $r_i > r_o$, it can be seen that rounding just the inlet edge has little influence on the result. On the contrary, rounding the outlet edge results in changes both in the peak absorption frequency and the absorption magnitude and gives a result similar to the panel with both

edges rounded. In Fig. 5.5d, one can notice no difference in the results between only the inlet and only the outlet edges rounded. The conclusion can be that what influences the outcome is the angle between the perforation surface and the panel surface. In the case of straight perforation, when both of these angles are right, the influence of rounding the edges is the same. Meanwhile, in the case of a tapered perforation, where one angle is acute and the other obtuse, rounding the acute angle results in a more significant change in absorption magnitude and frequency.

5.1.5. Hourglass-shaped perforations

In Fig. 5.6a, the absorption curves for three pairs of panels are shown. Each pair consists of a panel with hourglass-shaped perforations and a panel with inverse-hourglass-shaped perforations, and their smaller and larger radius are the same. The absorption peaks are at lower frequencies for the inverse-hourglass geometry compared to the panels with hourglass perforations. A comparison of absorption coefficients for the panels of different types in Fig. 5.6b shows that The panel with tapered perforations gives an absorption peak located in-between the peaks resulting from the hourglass- and the inverse-hourglass geometries.
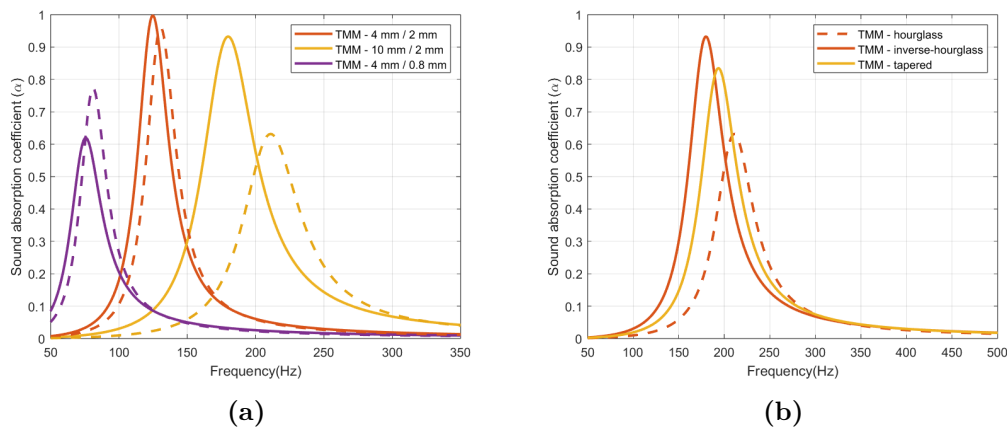
Figure 5.6: (a) Absorption coefficient of panels with hourglass- (dashed line) and inverse-hourglass-shaped (solid line) perforations; (b) Comparison of absorption coefficients of different types of panels. The geometrical characteristics of the panels are shown in Table A.5 in Appendix A.

5.1.6. Bubble-shaped perforations

A rounded expansion in the perforation results in an absorption curve similar to that obtained for the inverse-hourglass-shaped perforation (see Fig. 5.7). Although the peak is at a lower frequency, the difference is marginal.
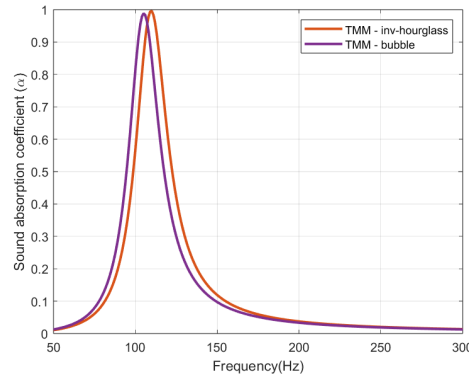
Figure 5.7: Absorption coefficient of panels with bubble-shaped perforations and hourglass-shaped perforations, geometrical characteristics of the system are shown in Table A.6 in Appendix A.

5.1.7. Perforations with embedded resonant structures

Panels with embedded resonators were analysed with FE models. The results show that adding resonant structures with necks connected to the perforation creates a coupled system with additional absorption peaks. The results for each system are shown in sections 5.1.7.1 and 5.1.7.2.

5.1.7.1. Torus-shaped resonator

An absorber consisting of a panel with an embedded resonator, an air gap, and rigid backing results in a structure where two resonances occur. This behaviour can be seen in Fig. 5.8. The first peak corresponds to the resonance of the system consisting of the perforation and the air gap. The other peak is related to the resonance of the embedded structure. In Fig. 5.9, the sound pressure levels in the model are shown at peak frequencies.
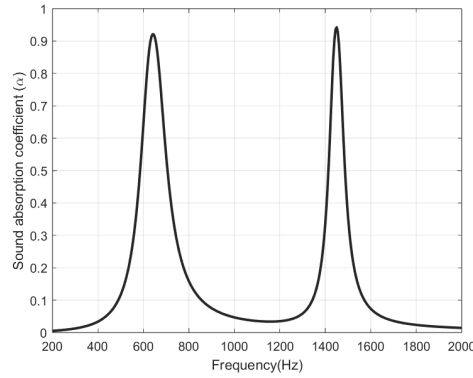
Figure 5.8: Absorption coefficient of a panel with a torus-shaped resonator embedded in its thickness, geometrical characteristics of the system are shown in Table A.7 in Appendix A.

Two parametric studies were carried out to investigate the influence of the perforation radius r and the embedded torus inner radius r_{HR}. In Fig. 5.10a, it can be seen that the radius of the torus only influences one of the absorption peaks. The peak corresponding to the air gap does not change. However, in Fig. 5.10b, the coupled behaviour of the system is visible, as with the changes in the perforation radii, both absorption peaks are altered.

(a)   (b)
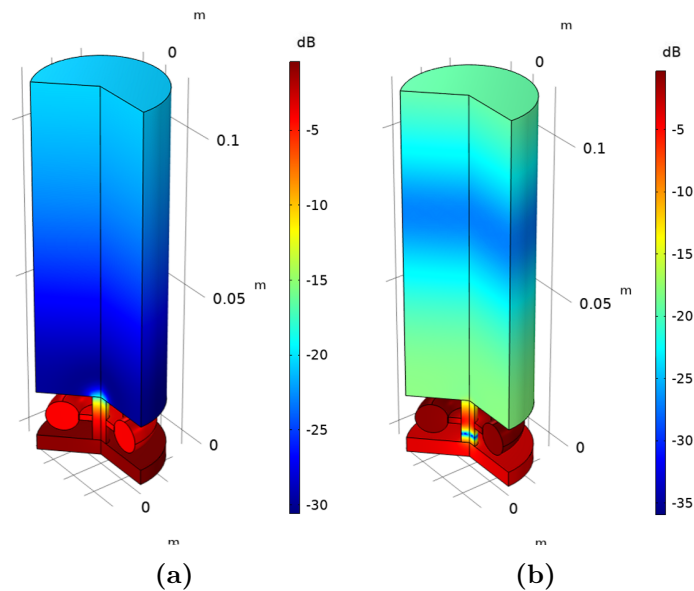
Figure 5.9: Sound pressure distribution in the system at frequencies: (a) 642 Hz, (b) 1450 Hz.
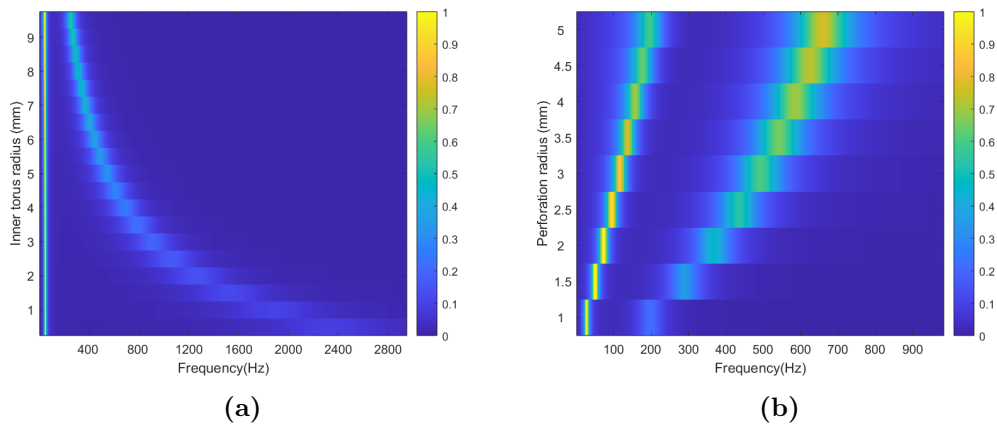
Figure 5.10: Sound absorption of a panel with embedded torus-shaped resonator as a function of (a) embedded torus' radii; (b) perforation radius. The geometrical characteristics of the analysed panels are shown in Table A.7 in Appendix A.

5.1.7.2. Spherical resonators

Similarly to the case of the torus-shaped resonator, introducing two pairs of differently-sized spherical resonators results in three absorption peaks (see Fig. 5.11). The first peak is related to the resonance of the air gap connected to the perforation, and the two following correspond to the two pairs of spheres. This can be seen in the pressure distributions at resonance frequencies shown in Fig. 5.12.
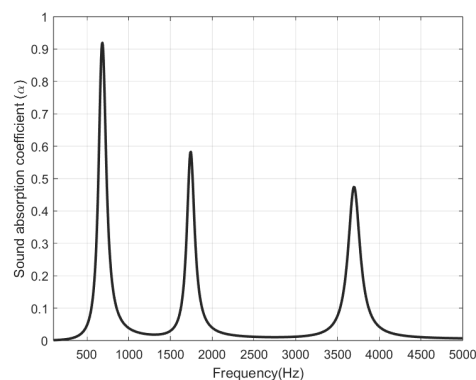
Figure 5.11: Absorption coefficient of a panel with four spherical resonators embedded in its thickness. The geometrical characteristics of the system are shown in Table A.8 in Appendix A.
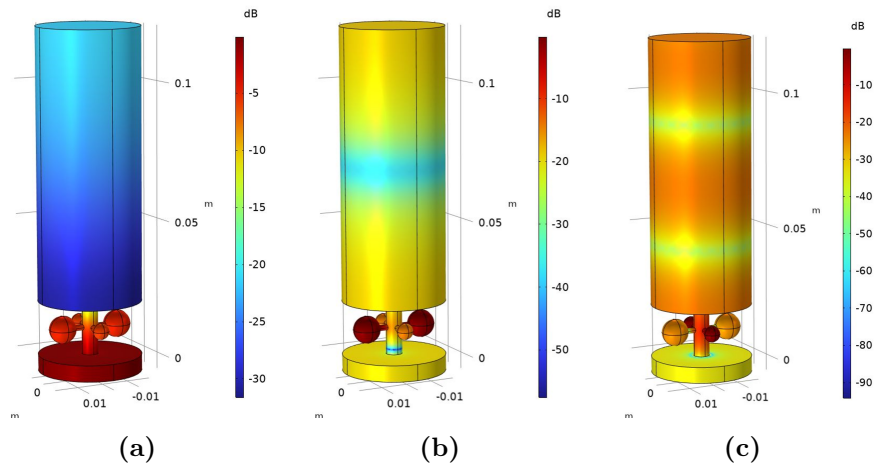
Figure 5.12: Sound pressure distribution in the system at frequencies: (a) 685 Hz, (b) 1740 Hz, (c) 3700 Hz.

Three parametric studies were performed to investigate the influence of the perforation radius and the embedded spheres' radii. In Figs. 5.13a and 5.13b the influence of increasing and decreasing the embedded resonators' radii is shown. When all spheres have the same radius, only two peaks occur. With increasing variation between the two pairs of resonators, the third peak emerges and becomes more significant. It can also be noticed that when the spheres are similar in size, a coupled effect occurs, and both peaks related to them change slightly. In Fig. 5.13c, the coupled behaviour of the system is shown: all three absorption peaks vary with the change in the perforation radius.
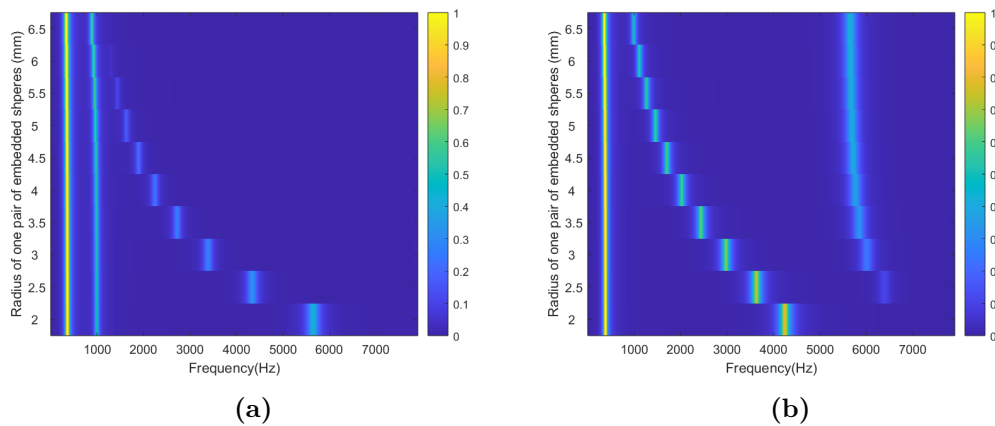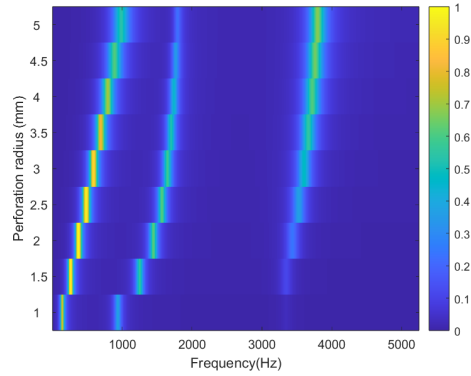
(c)

Figure 5.13: Sound absorption of a panel with embedded spherical resonators as a function of (a) and (b) embedded spheres' radii; (c) perforation radius. The geometrical characteristics of the panels are shown in Table A.8 in Appendix A.

5.2. Optimisation

As described in section 3.3, an optimisation algorithm was used to find the optimal panel design. The geometry with tapered perforations was optimised. To ensure just the shape of the perforation is influencing the absorption coefficient and not the cavity depth or perforation spacing, optimisation was performed for three parameters: inlet radius r_i, outlet radius r_o ($r_i \geq r_o$), and panel thickness t. Limit values of those variables are shown in Table 5.1. The cavity depth D was chosen to be 10 mm. As the optimisation was performed with the idea of producing samples for experimental validation, the perforation spacing was adjusted to the size of the impedance tube. The square-shaped unit cell size was 19.2 mm or 16.6 mm, corresponding to three or four perforations in one sample panel. The objective function was defined as $1 - \alpha_{avg}$, where α_{avg} is the average sound absorption over a given frequency band, in this case, over 500 Hz third-octave band and 1000 Hz third-octave band. A constraint function was introduced to account for the angle limit described in section 5.1.1: $(r_i - r_o)/t - \tan 25° \leq 0$. The geometrical characteristics of optimal panels are presented in Table A.9 in Appendix A.

Variable	Lower limit	Upper limit
$r_i (mm)$	1	10
$r_o (mm)$	1	10
t (mm)	5	20

Table 5.1: Limit values of optimisation variables

5.3. Experimental validation

To validate the proposed models, four samples for experimental tests were prepared. The samples were made using fused deposition modelling technology. Three models are the results of optimising tapered panels, and one is a panel with an embedded resonator with arbitrarily chosen dimensions. Samples were printed with Polylactic Acid (PLA) using Blocks One MKII 3D printer. The geometrical characteristics of the panels are detailed in Tables A.9 and A.10 in Appendix A, and the produced samples are shown in Figs. 5.14 and 5.15.

(a) (b) (c)
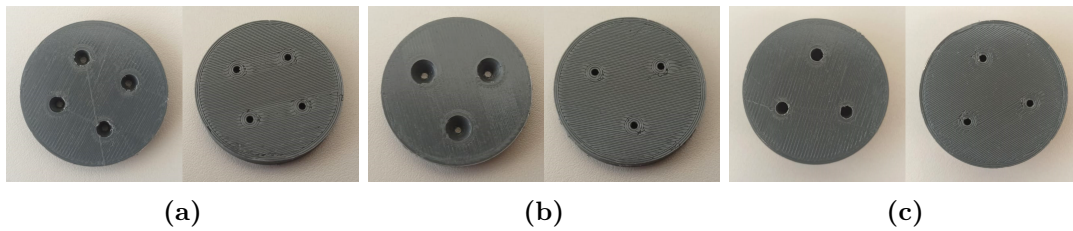
Figure 5.14: Top and bottom view of the samples: (a) panel 1; (b) panel 2; (c) panel 3.

Figure 5.15: View of panel 4 before and after assembly.

The experimental validation was done by measuring the normal incidence absorption coefficient of the samples using the method described in section 3.4. The impedance tube used had an inner diameter of 38 mm. The measurement set consisted of two G.R.A.S. 46 AE 1/2 CCP free-field microphones, a NI USB-4431 dynamic signal acquisition device and a

computer, where the registered signals were processed using MATLAB [39]. The system was excited with a random signal by a loudspeaker at one end of the tube.

Fig. 5.16 shows the results of the measurements along with the analytical and numerical results.
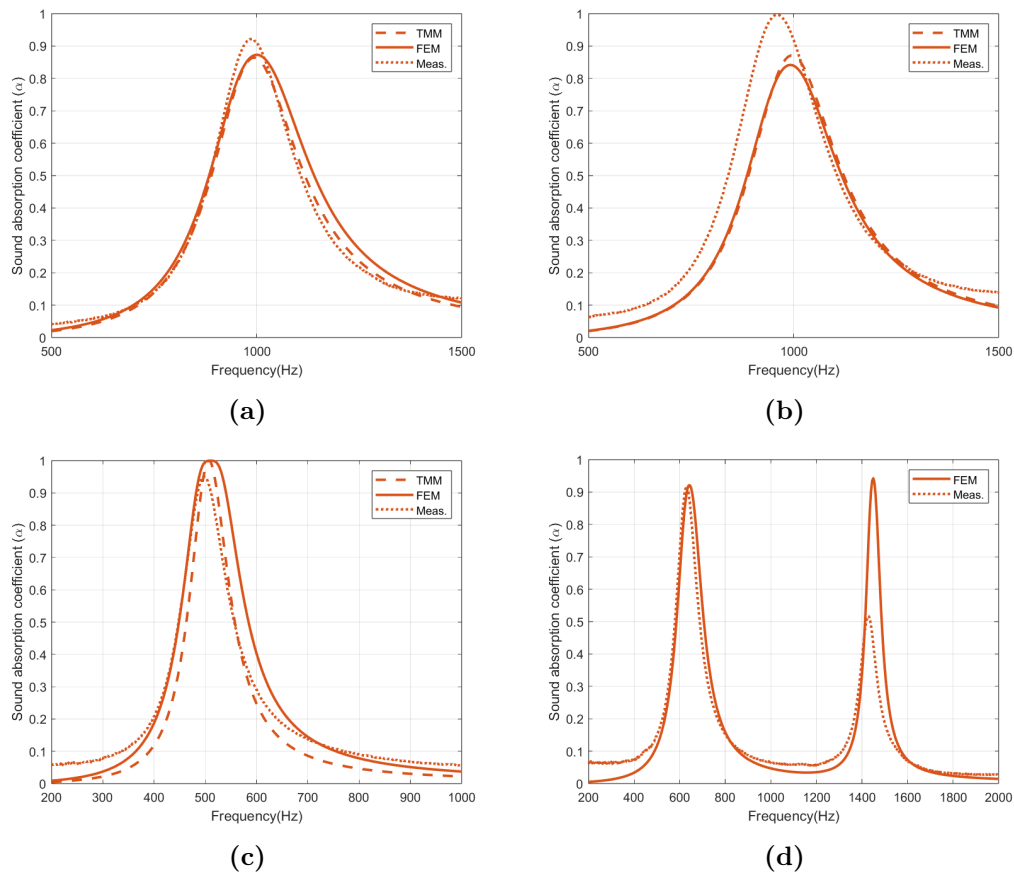
Figure 5.16: Experimental sound absorption coefficient compared to analytical and numerical: (a) panel 1; (b) panel 2; (c) panel 3; (d) panel 4.
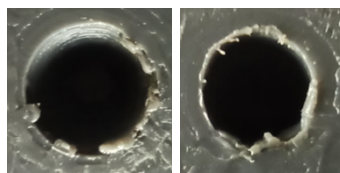
Figure 5.17: Examples of sample defects due to printing process imperfection.

The experimental results, compared to the analytical and numerical ones, are shown in

Fig. 5.16. In general, experimental results agree with analytical and numerical models. Both peak absorption frequencies and bandwidths are consistent with the predictions. The most considerable discrepancies can be seen in panels 2 and 4. In the case of panel 4, the second absorption peak is largely overestimated in the numerical predictions. Still, the coupled behaviour of the system with an embedded resonator is correctly predicted as the peak absorption frequencies coincide with the measured ones. The discrepancies between experimental results and prediction methods could be attributed to several reasons: the samples did not fit perfectly in the impedance tube, which resulted in air spaces between the panels and tube walls; the perforations were not perfectly circular (examples shown in Fig. 5.17; the perforations in each panel did not have precisely the same diameters; and the panel surfaces, including inside the perforations, were not smooth (this can be seen in Fig. 5.15). Those reasons can be mainly attributed to the 3D printing method. Due to those discrepancies, the supposition mentioned in section 5.1.1 of the tapered panels' behaviour being independent of flow direction could not be confirmed experimentally.

6. Conclusions and future work

Throughout this internship, perforated panels with various internal shapes and cross-sections were studied. Analytical and numerical tools were used to investigate diverse geometries. A model based on the transfer matrix method was developed to analyse panels with variable geometries. An optimisation procedure was applied to the tapered perforated panel to find the characteristics allowing for enhanced sound absorption. Experimental validation of the analytical and numerical models was carried out with the use of 3D-printed samples. The main conclusions from this project are summarized as follows:

- The influence of perforation cross-sectional characteristics and shapes on acoustic behaviour is significant and reaffirms the need for precise parameter control in perforated panel design. It was shown that changes in the internal geometry of a panel can result in shifting the absorption peak value and frequency and in the presence of additional peaks in the case of structures with embedded resonators.

- It is possible to finely tune the absorptive properties of perforated panels without impacting their aesthetic qualities. This is especially important in the context of practical applications of such panels.

- The fused deposition modelling 3D printing technology used in this project influenced the experimental results through added roughness and manufacturing inaccuracies. Although the experimental results generally showed good agreement with the analytical and numerical ones, a hypothesis of the tapered panels' absorptive properties being independent of flow direction could not be confirmed.

Future work can include:

- Developing an analytical model for tapered perforations with $\theta > 25°$ and investigation into the potential of such panels,

- Developing a TMM model for a panel with embedded resonators, which would allow for fast optimisation.

- Further investigation of the potential of embedded resonators.

- Analysis of possibilities and performance of combining different types of perforations in one panel.

Bibliography

[1] T. Cox and P. D'Antonio, *Acoustic Absorbers and Diffusers: Theory, Design and Application.* CRC Press, 3 ed., 2016.

[2] K. Attenborough and I. L. Vr, "Sound-absorbing materials and sound absorbers," in *Noise and Vibration Control Engineering*, pp. 215–277, John Wiley Sons, Inc.

[3] J. W. Strutt, *The Theory of Sound.* Cambridge University Press, 2011.

[4] U. Ingard, "On the theory and design of acoustic resonators," *The Journal of the Acoustical Society of America*, vol. 25, pp. 1037–1061, 1953.

[5] C. Zwikker and C. W. Kosten, *Sound absorbing materials.* Elsevier Pub. Co., 1949. Includes bibliographical references and indexes.

[6] P. M. Morse and K. U. Ingard, *Theoretical acoustics.* New York: McGraw-Hill, 1968.

[7] I. B. Crandall, *Theory Of Vibrating Systems And Sound.* D. Van Nostrand Company, 1926.

[8] J. F. Allard and N. Atalla, *Propagation of Sound in Porous Media.* Wiley, 2009.

[9] D.-Y. Maa, "Theory and design of microperforated panel sound-absorbing constructions," *Scientia Sinica*, vol. 18, pp. 55–71, 1975.

[10] R. H. Bolt, "On the design of perforated facings for acoustic materials," *The Journal of the Acoustical Society of America*, vol. 19, pp. 917–921, 1947.

[11] U. Ingård and R. H. Bolt, "Absorption characteristics of acoustic material with perforated facings," *The Journal of the Acoustical Society of America*, vol. 23, pp. 533–540, 1951.

[12] D.-Y. Maa, "Microperforated-panel wideband absorbers," *Noise Control Engineering Journal*, vol. 29, p. 77, 1987.

[13] M. R. Stinson, "The propagation of plane sound waves in narrow and wide circular tubes, and generalization to uniform tubes of arbitrary cross-sectional shape," *The Journal of the Acoustical Society of America*, vol. 89, pp. 550–558, 1991.

[14] N. Atalla and F. Sgard, "Modeling of perforated plates and screens using rigid frame porous models," *Journal of Sound and Vibration*, vol. 303, pp. 195–208, 2007.

[15] D. Li, D. Chang, and B. Liu, "Enhancing the low frequency sound absorption of a perforated panel by parallel-arranged extended tubes," *Applied Acoustics*, vol. 102, pp. 126–132, 2016.

[16] J. Carbajo, J. Ramis, L. Godinho, and P. Amado-Mendes, "Perforated panel absorbers with micro-perforated partitions," *Applied Acoustics*, vol. 149, pp. 108–113, 2019.

[17] K. H. Kim and G. H. Yoon, "Absorption performance optimization of perforated plate using multiple-sized holes and a porous separating partition," *Applied Acoustics*, vol. 120, pp. 21–33, 2017.

[18] J. Carbajo, S. G. Mosanenzadeh, S. Kim, and N. X. Fang, "Sound absorption of acoustic resonators with oblique perforations," *Applied Physics Letters*, vol. 116, p. 054101, 2020.

[19] T. Dupont, P. Leclaire, R. Panneton, and O. Umnova, "A microstructure material design for low frequency sound absorption," *Applied Acoustics*, vol. 136, pp. 86–93, 2018.

[20] J. Carbajo, J. Ramis, L. Godinho, and P. Amado-Mendes, "Modeling of grooved acoustic panels," *Applied Acoustics*, vol. 120, pp. 9–14, 2017.

[21] R. Sailesh, L. Yuvaraj, M. Doddamani, L. B. M. Chinnapandi, and J. Pitchaimani, "Sound absorption and transmission loss characteristics of 3d printed bio-degradable material with graded spherical perforations," *Applied Acoustics*, vol. 186, p. 108457, 2022.

[22] X. Liu, C. Yu, and F. Xin, "Gradually perforated porous materials backed with helmholtz resonant cavity for broadband low-frequency sound absorption," *Composite Structures*, vol. 263, p. 113647, 2021.

[23] X. Li, B. Liu, and C. Qin, "A perforated plate with stepwise apertures for low frequency sound absorption," *Applied Sciences*, vol. 11, p. 6180, 2021.

[24] M. Pereira, J. Carbajo, L. Godinho, J. Ramis, and P. Amado-Mendes, "Improving the sound absorption behaviour of porous concrete using embedded resonant structures," *Journal of Building Engineering*, vol. 35, p. 102015, 2021.

[25] K. Sakagami, M. Morimoto, M. Yairi, and A. Minemura, "A pilot study on improving the absorptivity of a thick microperforated panel absorber," *Applied Acoustics*, vol. 69, pp. 179–182, 2008.

[26] T. Herdtle, J. S. Bolton, N. N. Kim, J. H. Alexander, and R. W. Gerdes, "Transfer impedance of microperforated materials with tapered holes," *The Journal of the Acoustical Society of America*, vol. 134, pp. 4752–4762, 2013.

[27] R. T. Randeberg, *Perforated Panel Absorbers with Viscous Energy Dissipation Enhanced by Orifice Design*. PhD thesis, Department of Telecommunications, Norwegian University of Science and Technology, Trondheim, 2000.

[28] R. Sailesh, L. Yuvaraj, J. Pitchaimani, M. Doddamani, and L. B. M. Chinnapandi, "Acoustic behaviour of 3d printed bio-degradable micro-perforated panels with varying perforation cross-sections," *Applied Acoustics*, vol. 174, p. 107769, 2021.

[29] N. Jiménez, J.-P. Groby, and V. Romero-García, "The transfer matrix method in acoustics," in *Acoustic Waves in Periodic Structures, Metamaterials, and Porous Media*, pp. 103–164, 2021.

[30] J. Smits and C. Kosten, "Sound absorption by slit resonators," *Acustica*, vol. 1, pp. 114–122, 1951.

[31] Y. Miki, "Acoustical properties of porous materials. modifications of delany-bazley models.," *Journal of the Acoustical Society of Japan (E)*, vol. 11, pp. 19–24, 1990.

[32] *COMSOL Multiphysics® v. 5.6.* Stockholm, Sweden.: COMSOL AB.

[33] M. Berggren, A. Bernland, and D. Noreland, "Acoustic boundary layers as boundary conditions," *Journal of Computational Physics*, vol. 371, pp. 633–650, 2018.

[34] P. Gill, W. Murray, and M. Wright, *Practical Optimization.* Academic Press, 1981.

[35] R. H. Byrd, M. E. Hribar, and J. Nocedal, "An interior point algorithm for large-scale nonlinear programming," *SIAM Journal on Optimization*, vol. 9, no. 4, pp. 877–900, 1999.

[36] *Optimization Toolbox version: 9.5 (R2023a).* Natick, Massachusetts, United States: The MathWorks Inc.

[37] "ISO 10534-2: Acoustics - Determination of sound absorption coefficient and impedance in impedance tubes Part 2: Transfer Function Method," Standard ISO 10534-2:1998, International Organization for Standardization, Geneva, CH, 1998.

[38] R. L. Hardy, "Multiquadric equations of topography and other irregular surfaces," *Journal of Geophysical Research (1896-1977)*, vol. 76, no. 8, pp. 1905–1915, 1971.

[39] *Matlab version: 9.0 (R2016a).* Natick, Massachusetts, United States: The MathWorks Inc.

A. Geometrical characteristics of analysed panels

This appendix contains all the geometrical properties of the analysed perforated panels.

Figure	$r_i(mm)$	$r_o(mm)$	$\theta(°)$	t (mm)	D (mm)	a (mm)
	4	2	11	10	10	50
5.1 (a)	6	2	22	10	10	50
	8	2	31	10	10	50
	3	1	15	7.5	10	50
	4	1	22	7.5	10	50
5.1 (b)	5	1	28	7.5	10	50
	6	1	34	7.5	10	50
5.2 (a)	10	2	15	30	50	50
	10	9	2	30	50	50
5.2 (b)	10	2	15	30	50	50
	2	10	15	30	50	50

Table A.1: Geometrical characteristics of panels with tapered circular perforations

Figure	$r_i(mm)$	$r_o(mm)$	$\theta(°)$	t (mm)	D (mm)	a (mm)
5.3 (a)	4	2	22	5	20	50
5.3 (b)	3	3	0	5	20	50

Table A.2: Geometrical characteristics of panels with tapered and straight circular perforations and the air cavity filled with a porous material

Figure	$r_i(mm)$	$r_o(mm)$	$\theta(°)$	t (mm)	D (mm)	a (mm)
5.4 (a)	2	0.5	10	8	30	80
	4	2	14	8	30	80
5.4 (b)	2	0.5	10	8	30	80
	0.5	2	10	8	30	80

Table A.3: Geometrical characteristics of panels with tapered slits

Figure	$r_i(mm)$	$r_o(mm)$	$\theta(°)$	$r_{fill-i}(mm)$	$r_{fill-o}(mm)$	t (mm)	D (mm)	$r_{panel}(mm)$
5.5 (a)	10	2	15	-	-	30	50	28.8
	10	2	15	5	1	30	50	28.8
	10	2	15	7.5	1.5	30	50	28.8
5.5 (b)	2	2	0	-	-	30	50	28.8
	2	2	0	1.5	1.5	30	50	28.8
	2	2	0	4	4	30	50	28.8
5.5 (c)	10	2	15	-	-	30	50	28.8
	10	2	15	20	4	30	50	28.8
	10	2	15	20	-	30	50	28.8
	10	2	15	-	4	30	50	28.8
5.5 (d)	2	2	0	-	-	30	50	28.8
	2	2	0	4	4	30	50	28.8
	2	2	0	4	-	30	50	28.8
	2	2	0	-	4	30	50	28.8

Table A.4: Geometrical characteristics of panels with rounded edges

Figure	$r_i(mm)$	$r_o(mm)$	$r_{max}(mm)$	$r_{min}(mm)$	t (mm)	D (mm)	a (mm)
5.6 (a)	4	4	-	2	30	50	50
	2	2	4	-	30	50	50
	10	10	-	2	30	50	50
	2	2	10	-	30	50	50
	4	4	-	0.8	30	50	50
	0.8	0.8	4	-	30	50	50
5.6 (b)	10	10	-	2	30	50	50
	2	2	10	-	30	50	50
	10	2	-	-	30	50	50

Table A.5: Geometrical characteristics of panels with the hourglass- and inverse-hourglass-shaped perforations

Figure	$r_i(mm)$	$r_o(mm)$	$r_{max}(mm)$	t (mm)	D (mm)	a (mm)
5.7	2	2	3	30	50	50
	2	2	3	30	50	50

Table A.6: Geometrical characteristics of panels with inverse-hourglass- and bubble-shaped perforations

Figure	r (mm)	$r_{HR}(mm)$	$l_{HR}(mm)$	$w_{HR}(mm)$	t (mm)	D (mm)	$r_{panel}(mm)$
5.8	2.5	5	4	2	15	5	19
5.10 (a)	2	0.5-9.5	5	1	30	50	50
5.10 (b)	1-5	8	5	1	30	50	50

Table A.7: Geometrical characteristics of panels with embedded torus-shaped resonators

Figure	r (mm)	$r_{HR1}(mm)$	$r_{HR2}(mm)$	$l_{HR}(mm)$	$w_{HR}(mm)$	t (mm)	D (mm)	$r_{panel}(mm)$
5.11	3	3	5	3	1	20	5	19
5.13 (a)	2	2	2-6.5	3	1	20	5	19
5.13 (b)	2	6.5	2-6.5	3	1	20	5	19
5.13 (c)	1-5	3	5	3	1	20	5	19

Table A.8: Geometrical characteristics of panels with embedded spherical resonators

Sample	$r_i(mm)$	$r_o(mm)$	$\theta(°)$	t (mm)	D (mm)	a (mm)
Panel 1	2.2	1.0	13	5.0	10	16.6
Panel 2	3.2	1.0	24	5.0	10	19.2
Panel 3	1.7	1.1	2	15.3	10	19.2

Table A.9: Geometrical characteristics of the optimised panels with tapered perforations

Sample	r (mm)	$r_{HR}(mm)$	$l_{HR}(mm)$	$w_{HR}(mm)$	t (mm)	D (mm)	$r_{panel}(mm)$
Panel 4	2.5	5	4	2	15	5	19

Table A.10: Geometrical characteristics of the 3D-printed panel with an embedded torus-shaped resonator